Supplementary material to the paper:
Synergy of Using Nadir and Limb Instruments for Tropospheric Ozone Monitoring

Viktoria F. Sofieva[1], Risto Hänninen[1], Mikhail Sofiev[1], Monika Szelag[1], Hei Shing Lee[1], Johanna Tamminen[1], Christian Retscher[2]

[1]Finnish Meteorological Institute, Helsinki, Finland
[2]ESA/ESRIN, Frascati, Italy

Correspondence to: Viktoria F. Sofieva (viktoria.sofieva@fmi.fi)

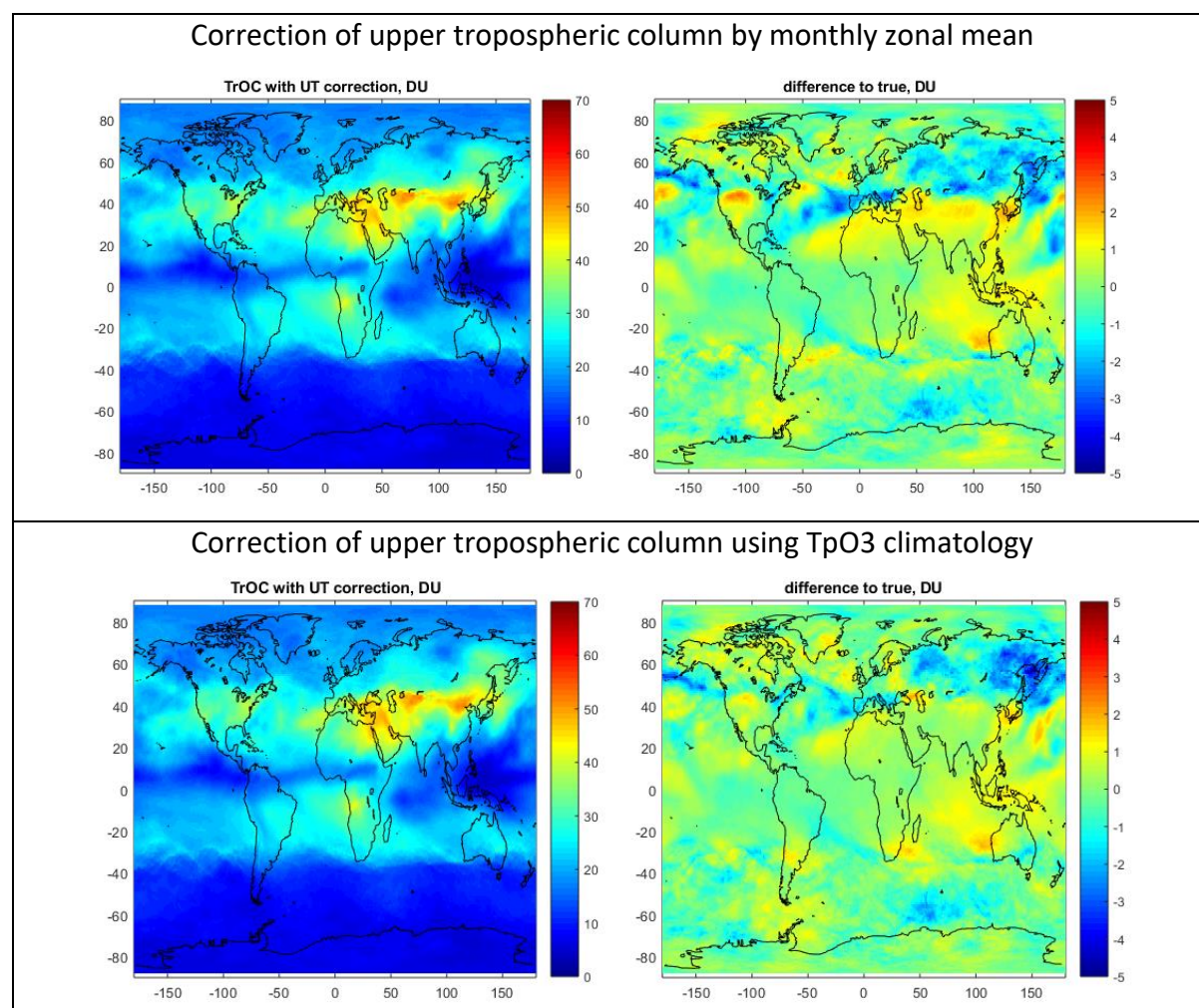## S1.   Feasibility studies on residual method to retrieve tropospheric ozone

Figure S1. Illustration of correction by UT when the upper tropospheric ozone is estimated using monthly mean values (top) and using the tropopause-related ozone climatology (bottom). Left panels: estimated truncated TrOC for July 2008, right: difference to true truncated TrOC.
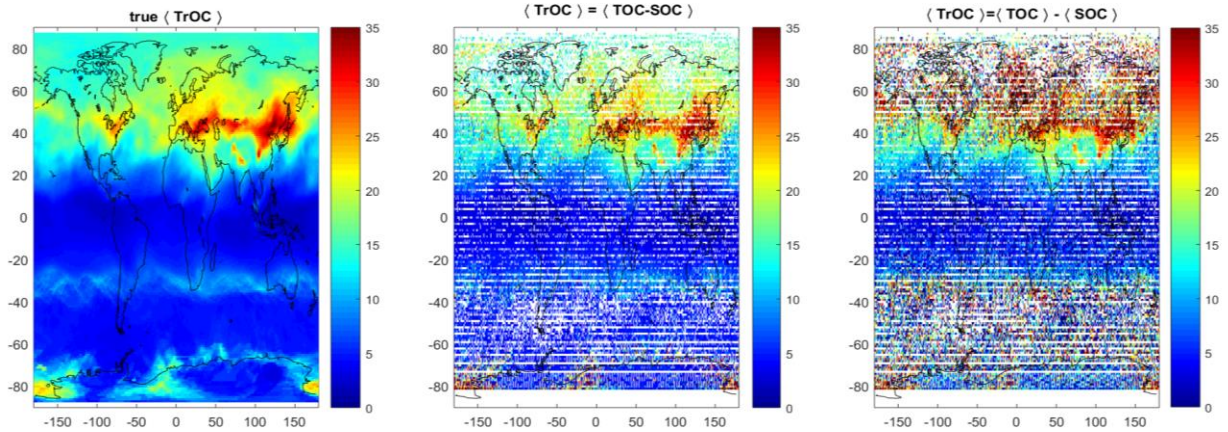
Figure S2. "True" monthly average tropospheric ozone column $\langle \text{TrOC} \rangle$ for July 2008 from the full SILAM field (left), $\langle \text{TrOC} \rangle = \langle \text{TOC} \rangle - \langle \text{SOC} \rangle$ (right), and the TrOC computed using the daily data $\langle \text{TrOC} \rangle = \langle \text{TOC - SOC} \rangle$ (center).
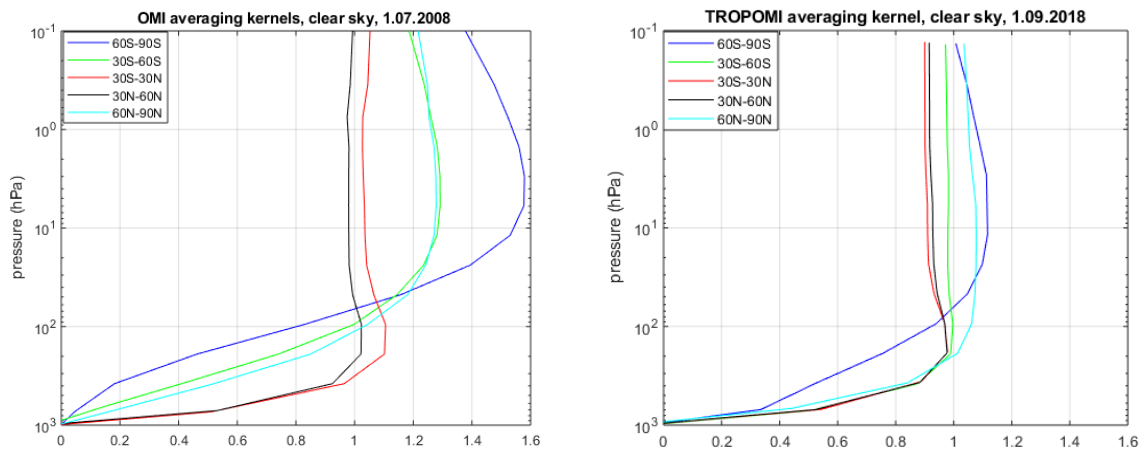

Figure S3. Left: typical OMI averaging kernels for clear-sky conditions (example for 1 July 2008). Right: TROPOMI typical averaging kernels for clear-sky conditions (example for 1 September 2018).
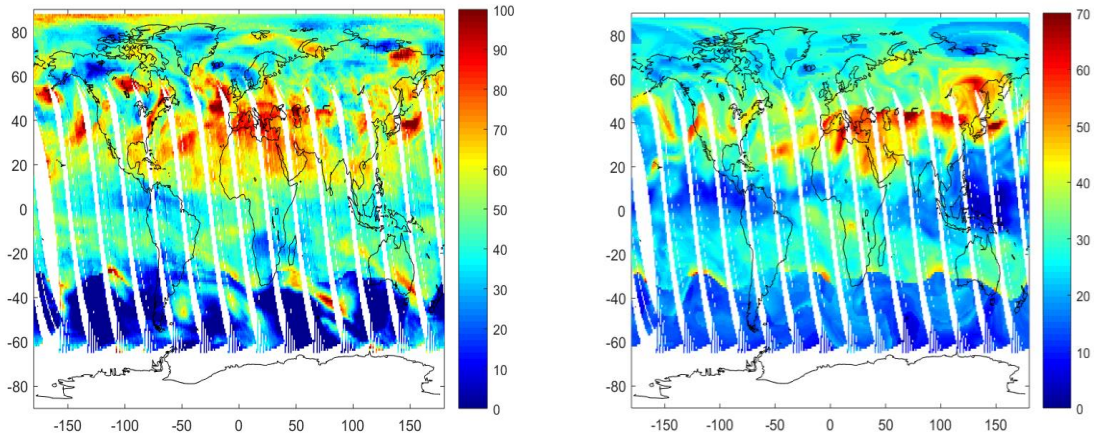
Figure S4. Tropospheric ozone column (from ground to tropopause) 1 July 2008 evaluated using SILAM data. Left – full space-time colocation with OMI, right – daily mean at OMI locations.

S2.   Adjusted SILAM ozone field

The simulated ozone field by the chemistry-transport model is an attractive source of information for various feasibility and sensitivity studies. This additional source of information is of especial importance in the UTLS, where the accuracy of satellite data is rather poor and the covered altitude range is not uniform over the globe. It is instrument-specific, therefore the resulting fields solely based on retrievals may be not accurate.

The SILAM model has proved to produce realistically distribution of ozone field, including the special events like ozone hole and mini-holes (Sofiev et al., 2020), https://en.ilmatieteenlaitos.fi/news/1140594517; https://en.ilmatieteenlaitos.fi/tiedote/1276664372, visited 03.07.2021). In addition, we have studied the small-scale ozone variability by the structure function method using OMI and SILAM total ozone column data and have found that they are in a very good agreement (Supplement, Sect S3). However, the model field is biased with respect to satellite data.

One possible approach to make the model data consistent with observations is data assimilation but this approach is critically dependent on the amount of data used for assimilation. In particular, changing satellite missions can affect the long-term stability of the assimilated data. We apply a different approach: we adjust SILAM data to MLS observation by computing space-resolving daily biases. These biases are evaluated as a weighted mean of model deviations from the observations in 10°x30° latitude-longitude bin, for each pressure level and each grid-point. As an example, MLS observations, original SILAM data, and the adjusted SILAM data for 20 June 2018 are shown in Figure S5.

The size of latitude-longitude box for evaluation of SILAM bias is relatively large, so that the small-scale structure of the model field is preserved in the adjusted field. For example, one can notice interesting small-scale perturbations in Figure S5.

3

The uncertainty associated with the bias correction is estimated as the interpolated absolute difference between MLS and SILAM adjusted data. In majority of locations, the estimated uncertainty is a few percent (an example is shown in Figure S5, right bottom panel).
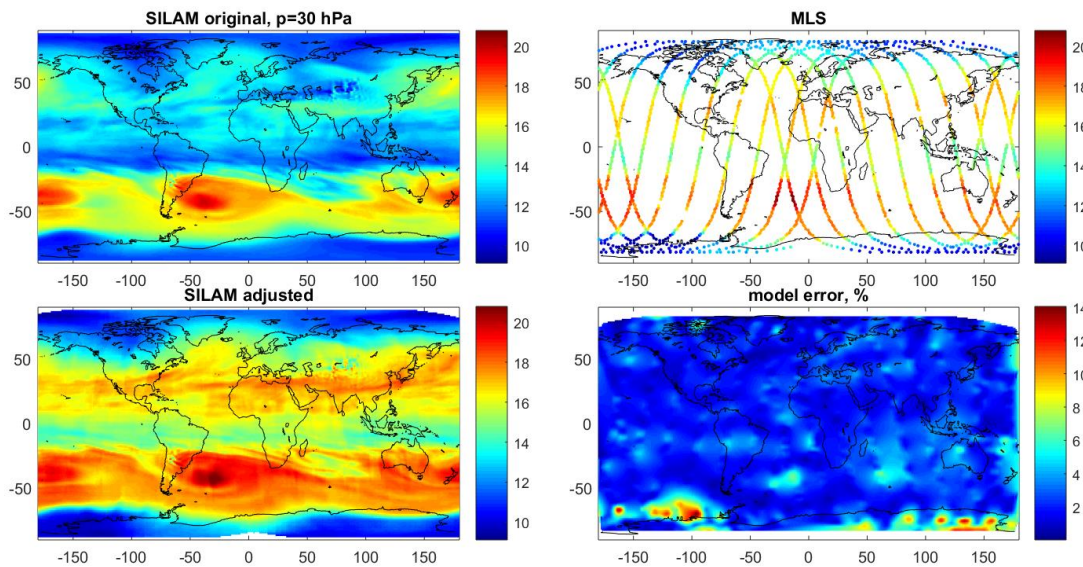

Figure S5. Ozone (DU/km) at 30 hPa on 20 June 2018 from original SILAM data (left top), MLS observation (right top), adjusted SILAM data (left bottom). The uncertainties associated with adjusted SILAM data are shown on right bottom panel.
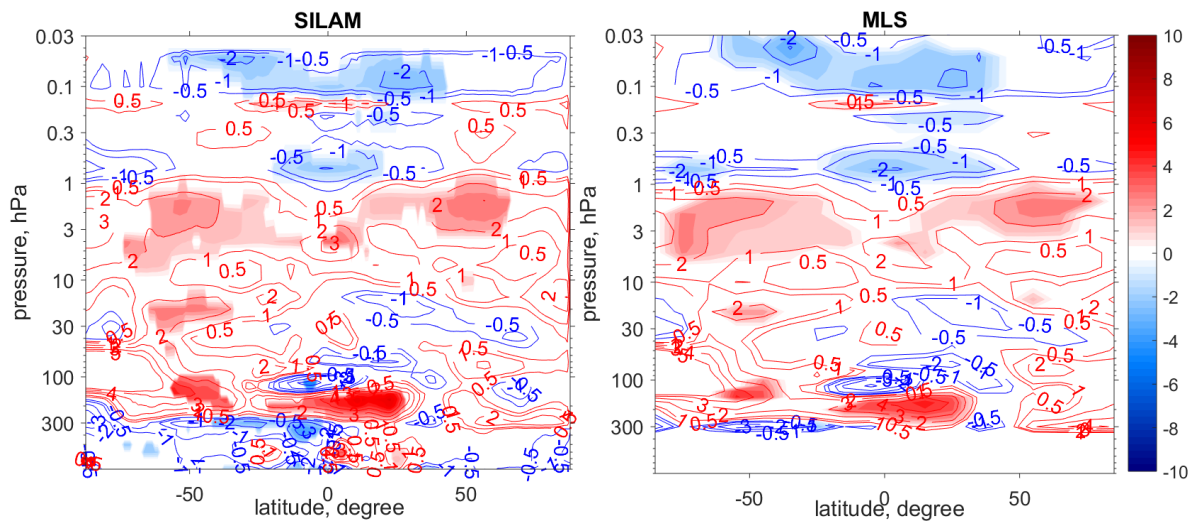

Figure S6. Ozone trends (% dec^{-1}) in 2004-2018 as a function of latitude and altitude. Ozone trends are evaluated via multiple linear regression (Sofieva et al., 2017; 2020b) using adjusted SILAM ozone profiles (left) and MLS data (right). All trends are shown by colored contours, while the statistically significant at 95% level trends are shown by shades.

Compared to the data assimilation methods, the model is much tighter nudged to the observations, so that the potentially wrong trends in the model do not affect the resulting dataset. At the same time, changes in the data availability do not affect the very smooth bias corrections as long as the varying amount of retrievals do not bring any systematic bias themselves. This is illustrated in Figure S6, which compares the zonal mean ozone trends in 2004-2018 from MLS and from adjusted SILAM dataset. As observed in Figure S6, these trends are nearly identical, as expected.

Since MLS profiles are recommended for use at altitudes above 250 hPa, we apply a fast 3 –point linear transition to original SILAM ozone profiles at lower altitudes: at 250 hPa, the adjusted model is used, at next level below (300 hPa) – the mean of original and adjusted data, and 350 hPa and below – original SILAM data. This step is justified by a more extensive evaluation of SILAM in the troposphere than in the stratosphere (see, e.g., Copernicus regional evaluation at https://atmosphere.copernicus.eu/index.php/regional-services, visited 03.07.2021, in particular, evaluation at elevated stations (Douros et al., 2021), first approaches to evaluation in Asia (Brasseur et al., 2019; Petersen et al., 2019), etc.).

S3.   Analysis of small-scale ozone variability using OMI and SILAM data

For the analyses, we used SILAM daily-mean ozone fields and OMI data. For selection of the tropospheric and the stratospheric ozone columns, we used the thermal tropopause/ozonepause definition as described in the main text. The OMI retrievals were gridded with 1° x 1° resolution. It was assumed that the stratospheric ozone column in the retrievals corresponds to the cloudy conditions, i.e. we used columns where clouds overshadowed the tropospheric part.

All ozone columns - total, stratospheric and tropospheric - have large temporal variability. Analogously to (Sofieva et al., 2021), we characterized the variability of the ozone field by the structure function (Tatarskii, 1961):

$$D(\boldsymbol{\rho}) = D(\mathbf{r}_1 - \mathbf{r}_2) = \left\langle \left[f(\mathbf{r}_1) - f(\mathbf{r}_2) \right]^2 \right\rangle, \quad (1)$$

where $\mathbf{r}_1$ and $\mathbf{r}_2$ are two locations and $\boldsymbol{\rho} = \mathbf{r}_1 - \mathbf{r}_2$. This concept assumes that the random field is locally homogeneous, which is the spatial equivalence of a random process with stationary increments. In spatial statistics, $D(\boldsymbol{\rho})$ is called the variogram (Wackernagel, 2003).

The structure functions in latitude and in longitude are evaluated for different seasons and broad latitude bands for years 2005-2017, for both total and stratospheric columns and experimental and simulated ozone fields. The TOC structure functions are shown in Figures S7 and S8, for OMI and SILAM data, respectively. The analogous structure functions for SOC are shown in Figures S9 and S10.
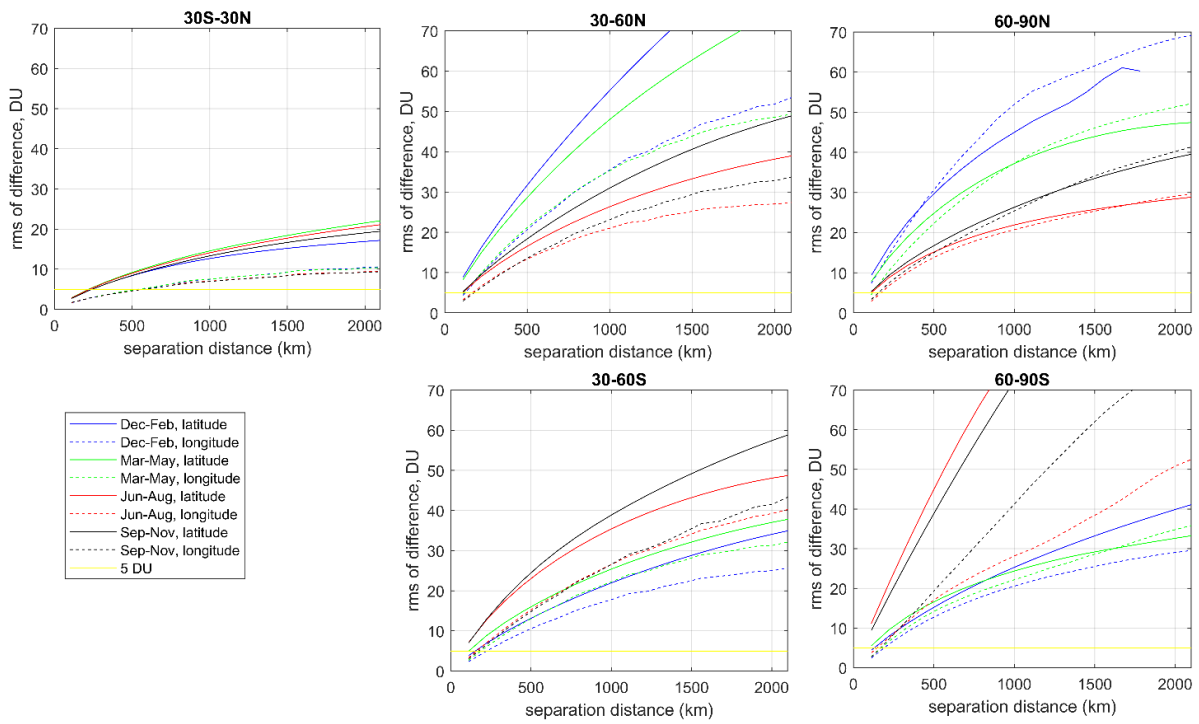
Figure S7. OMI TOC structure function, for different latitude bands and seasons. The horizontal yellow line corresponds to level 5 DU.
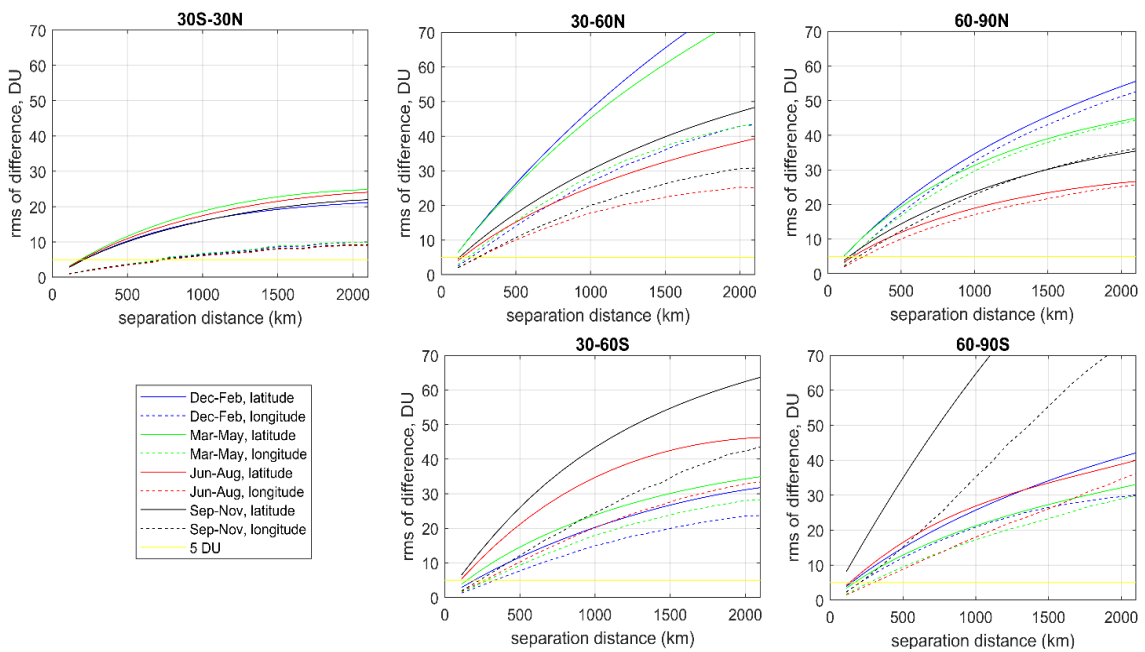

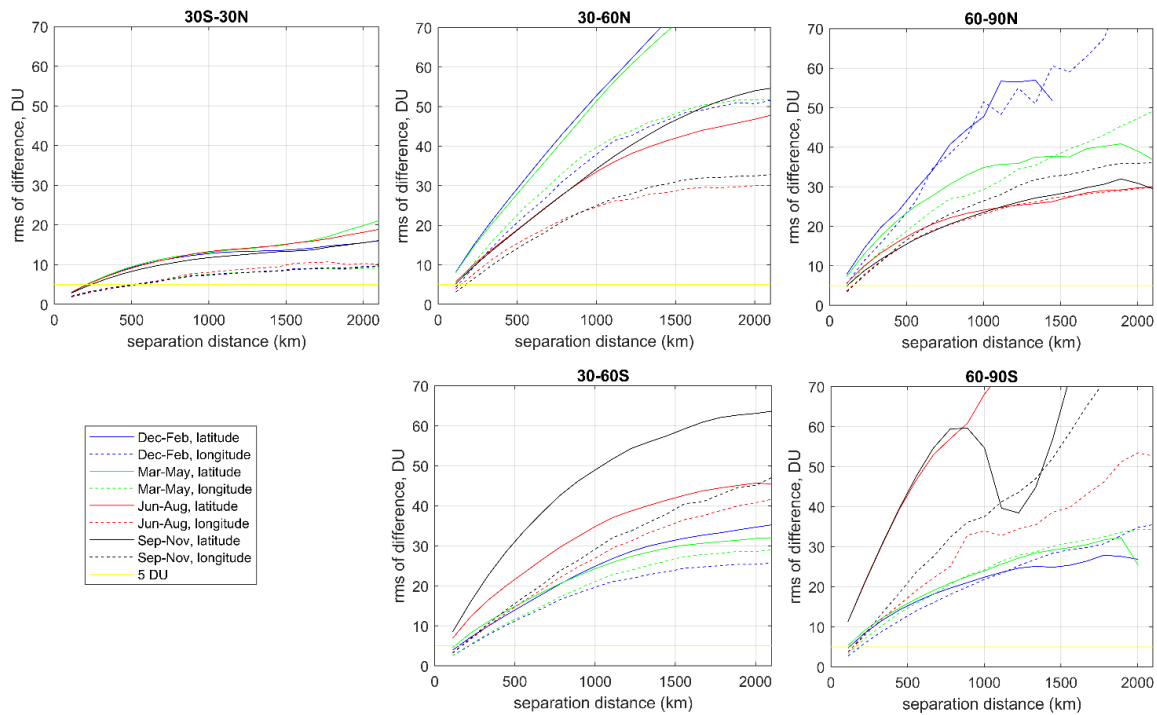*Figure S8. As Figure S7, but for SILAM TOC.*

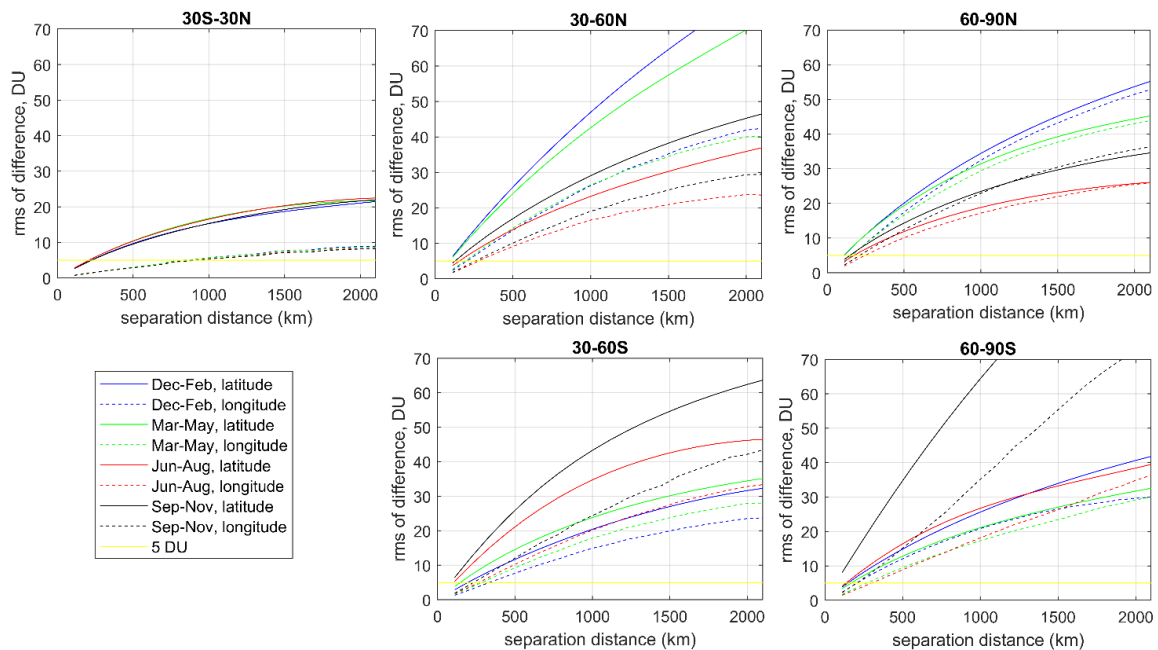*Figure S9. As Figure S7, but for SOC using OMI data.*

Figure S10 As Figure S7, but for SOC using SILAM data.

The obtained morphology of ozone variability is quite expected: it is overall much smaller in the tropics than at middle and high latitudes, where it has a pronounced seasonal cycle. In polar regions in winter and spring the ozone variability is very strong, even for small separations. The structure functions are evidently anisotropic nearly everywhere, with stronger variability in latitudinal direction. The only exceptions are latitudes 60-90 N in all

seasons and 60-90 S in March-May. As expected, the structure functions for total ozone and for stratospheric ozone look similar. The modelled and experimental data are in a very good agreement.

S4.   Uncertainties of the interpolated ozone profiles

The estimation of uncertainties associated with the interpolated dataset of ozone profiles are illustrated in Figure S11. Firstly, we used the error propagation to evaluated uncertainty after the kriging step (Figure S11, top right). In addition, we estimated the interpolation uncertainty using the SILAM data: we run the same interpolation but on the SILAM fields sub-sampled at the measurements locations, and evaluated the error as the absolute difference of true and interpolated data (Figure S11, bottom left). The final uncertainty is the root-mean-square of error propagation and model-assessed interpolation errors (Figure S11, bottom right).
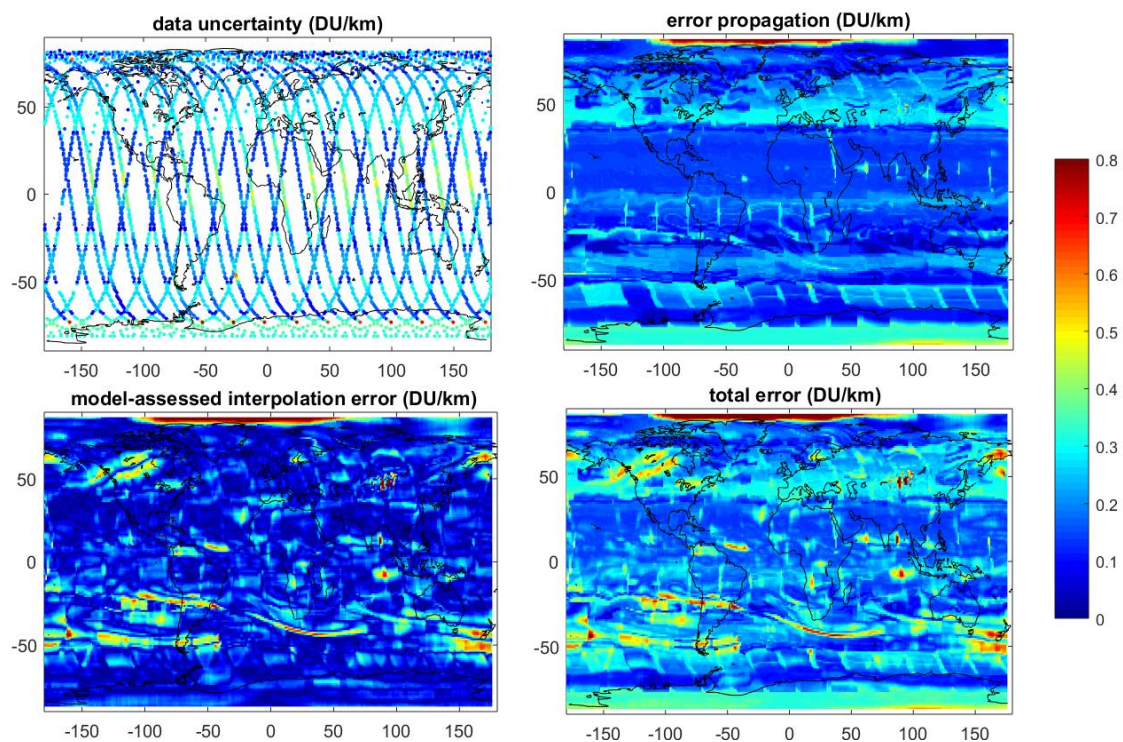

Figure S11. Illustration of uncertainty estimation of the interpolated ozone data. Data are for 1 Sep 2018, at 10 hPa. Top left: uncertainty of satellite data, top right: error propagation after kriging-type interpolation, bottom left: interpolation error from SILAM data, bottom right: total uncertainty.

S5. Compatibility of ozone data from limb and nadir instruments.

We compared OMI and TROPOMI measurements in cloudy conditions (the ghost column removed) with the integrated ozone profiles from the cloud-top height. For this comparison, we selected cloudy pixels with cloud fraction >0.8 and cloud-top pressure less than 350 hPa and the corresponding limb profiles from the SILAM adjusted field. The example of the comparison for September 2018 is shown in Figure S12.
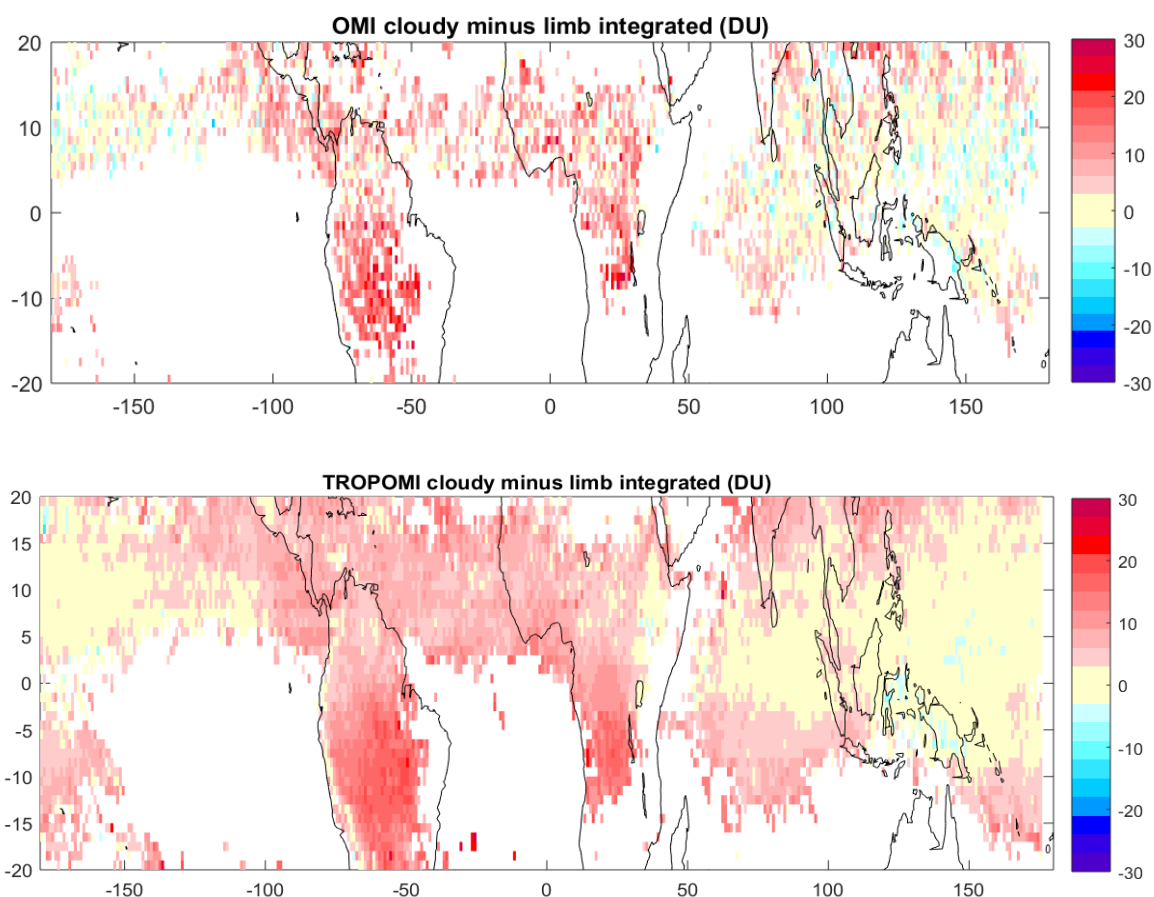

Figure S12. Total column in cloudy pixels from nadir instruments minus adjusted SILAM integrated from the cloud-top height, Sep 2018. Top: OMI, bottom: TROPOMI.

S6. References

Brasseur, G.P., Xie, Y., Petersen, A.K., Bouarar, I., Flemming, J., Gauss, M., Jiang, F., Kouznetsov, R., Kranenburg, R., Mijling, B., Peuch, V.-H., Pommier, M., Segers, A., Sofiev, M., Timmermans, R., van der A, R., Walters, S., Xu, J., Zhou, G., 2019. Ensemble forecasts of air quality in eastern China – Part 1: Model description and implementation of the MarcoPolo–Panda prediction system, version 1. Geosci. Model Dev. 12, 33–67. https://doi.org/10.5194/gmd-12-33-2019

Douros, J., Eskes, H.J., Akritidis, D., Antonakaki, T., Bennouna, Y., Blechschmidt, A.-M., Bösch, T., Clark, H., Gielen, C., Hendrick, F., Kapsomenakis, J., Kartsios, S., Katragkou,

E., Melas, D., Mortier, A., Peters, E., Petersen, K., Piters, A., Richter, A., van Roozendael, M., Schulz, M., Sudarchikova, N., Wagner, A., Zanis, P., Zerefos, C., 2021. Validation of CAMS regional services: concentrations above the surface - status update for September - November 2020. https://doi.org/10.24380/HZGZ-XY79

Petersen, A.K., Brasseur, G.P., Bouarar, I., Flemming, J., Gauss, M., Jiang, F., Kouznetsov, R., Kranenburg, R., Mijling, B., Peuch, V.-H., Pommier, M., Segers, A., Sofiev, M., Timmermans, R., van der A, R., Walters, S., Xie, Y., Xu, J., Zhou, G., 2019. Ensemble forecasts of air quality in eastern China – Part 2: Evaluation of the MarcoPolo–Panda prediction system, version 1. Geosci. Model Dev. 12, 1241–1266. https://doi.org/10.5194/gmd-12-1241-2019

Sofiev, M., Kouznetsov, R., Hänninen, R., Sofieva, V.F., 2020. Technical note: Intermittent reduction of the stratospheric ozone over northern Europe caused by a storm in the Atlantic Ocean. Atmospheric Chemistry and Physics 20, 1839–1847. https://doi.org/10.5194/acp-20-1839-2020

Sofieva, V.F., Lee, H.S., Tamminen, J., Lerot, C., Romahn, F., Loyola, D.G., 2021. A method for random uncertainties validation and probing the natural variability with application to TROPOMI on board Sentinel-5P total ozone measurements. Atmospheric Measurement Techniques 14, 2993–3002. https://doi.org/10.5194/amt-14-2993-2021

Tatarskii, V.I., 1961. Wave Propagation in a Turbulent Medium. McGraw-Hill, New York.

Wackernagel, H., 2003. Multivariate Geostatistics. Springer Verlag, Berlin Heidelberg.